International Journal of Mechanical Sciences 210 (2021) 106732

Contents lists available at ScienceDirect

International Journal of Mechanical Sciences

journal homepage: www.elsevier.com/locate/ijmecsci

Ultra-thin and broadband low-frequency underwater acoustic meta-absorber

Yanni Zhang [a,*], Li Cheng [b,*]

[a] Institute of Launch Dynamics, Nanjing University of Science and Technology, Nanjing, Jiangsu, China
[b] Department of Mechanical Engineering, The Hong Kong Polytechnic University, Hung Hom, Kowloon, Hong Kong, China

ARTICLE INFO

Keywords:
Acoustic metamaterial
Sound absorption
Broadband low-frequency
Underwater sound
Elastic plates scatterers
Ultrathin layers

ABSTRACT

Acoustic metamaterials with deep-subwavelength thickness have aroused increasing interests for potential applications in low-frequency sound and vibration control. Most reported metamaterials, however, are for airborne sound, with fewer for low-frequency waterborne sound absorption because of water's much longer wavelength, weaker dissipation and closer impedance to solids. Current underwater sound absorption (SA) approaches merely work at broadband high frequencies (typically above 2 kHz) or narrowband low frequencies (by introducing discrete narrowband spring-mass local resonators (LRs)). Herein, an ultra-thin meta-absorber is proposed to achieve broadband low-frequency underwater SA via inserting thin and thickness-graded circular-elastic-plate scatterers (CPSs) into an elastomer matrix. Capitalizing on the thickness gradient among the CPSs and a backing plate behind the elastomer, the proposed design entails continuous broadband LRs, enriches the content of both local and coupled resonance modes inside the meta-absorber unit and enhances the coupling among them, thus enabling high and quasi-perfect SA at multiple frequencies and broad low-frequency range with a deep sub-wavelength thickness. Notably, quasi-perfect SA (>0.97) is realized at 415 Hz with an absorber whose thickness is 1.7% of the sound wavelength. An optimized design yields excellent sound absorption (>0.9, 0.952 on average) in the low frequency range from 500 to 2000 Hz. Such broadband low-frequency SA is confirmed by experiments. This research offers a novel and effective solution to achieve broadband low-frequency underwater SA, which may open up a new avenue to broadband low-frequency sound control using sub-wavelength structures.

1. Introduction

Designing broadband low-frequency acoustic metamaterials with deep-subwavelength thickness is of great interest and significance for applications such as acoustic sensing, noise shielding and super-resolution imaging [1]. Especially, high-performance water-borne acoustic metamaterials are of paramount importance for underwater stealth by functioning as e.g. an underwater anechoic coating. However, most reported low-frequency metamaterials with deep-subwavelength are for airborne sound [2–9]. Unlike airborne sound, waterborne sound has much longer wavelength but lower dissipation. Besides, the much smaller impedance contrast between water and most solids prevents the latter from being treated as rigid as often assumed when designing airborne metamaterials, so that the acoustic-structural coupling can no longer be neglected [10]. Thus, underwater meta-structure designs are much more difficult than those for airborne sound. An ideal underwater acoustic absorber calls for two pre-requisites: a characteristic impedance closer to that of water and a sufficiently large loss. The former guarantees an effective entry of incident sound waves into the structure while the latter ensures a sufficient dissipation of the entered energy. For homogenous sound-absorbing materials, however, reflection coefficient is proportional to the loss factor [11], i.e. the larger the loss factor, the higher the reflection or the weaker the impedance matching. Hence, the impedance matching and the high dissipation requirement are two competing factors, which are difficult to conciliate in conventional homogenous materials.

To improve sound absorption (SA), various sound-absorbing structures have been introduced to the surface/inside of materials to provide resonant or non-resonant underwater SA. Typical examples include air cavities as monopole resonators [12–14], rigid inclusions as dipole resonators [15–17], embedded local resonators (LRs) [18,19], gradient index structures [20,21] and porous structures [22–24], etc. Although

* Corresponding authors.
E-mail addresses: yanni.zhang@njust.edu.cn (Y. Zhang), li.cheng@polyu.edu.hk (L. Cheng).

https://doi.org/10.1016/j.ijmecsci.2021.106732
Received 20 June 2021; Received in revised form 31 July 2021; Accepted 6 August 2021
Available online 11 August 2021

these structures can improve the SA to a certain extent, they show obvious deficiencies. For example, air cavity inclusions are vulnerable to resist hydrostatic pressure. Rigid inclusions enhance the overall structural strength at the expense of compromising low-frequency SA. Similarly, existing gradient index structures, despite their intrinsic broadband nature, also suffer from poor low-frequency performance. Embedding LRs into absorbing materials provides an alternative to achieving low-frequency SA at a sub-wavelength thickness scale through local resonance mechanism [25–27]. These LRs usually consist of softly coated heavy cores embedded into a hard matrix and can be regarded as single degree-of-freedom (DOF) mass-spring resonators. As such, their absorbing bandwidths are relatively narrow. Investigations suggest that applying layers of absorbing materials with single DOF LRs [26] or multilayered LRs [27] has limited effect on SA band broadening.

As an attempt to achieve wideband SA, Jiang et al. [28] introduced network structures into local resonant materials to form a phononic crystal called phononic glass, which demonstrates strong SA in 12–30 kHz at high hydrostatic pressure. They also introduced woodpile structure into locally resonant materials, yielding locally resonant bandgaps in different frequency ranges or broadened SA from 5 to 30 kHz [29]. Note the achieved SA still mainly applies to high frequencies. Efforts were also made to use rubber coating embedded with combined cavities and rigid inclusions/LRs to improve the SA and its bandwidth [30,31], with nevertheless limited success due to the relatively weak coupling among different scatterers. Wang et al. [32] fabricated a sound absorbing material by combining a carbon fiber honeycomb skeleton with a gradient cavity shaped polyurethane to produce broadband SA above 2400 Hz under a hydraulic pressure of 1.5 MPa. Reported works allude to the idea of introducing multiple yet continuous LRs into an elastic medium for multiple and broadband resonant absorption, as opposed to the narrow band absorption induced by multiple single DOF LRs. A prototype of a such structure was proposed by Zhang et al. [33] via inserting 1D thin elastic strips/beams of varying lengths into a viscoelastic layer. However, that work was limited to a two-dimensional (2D) conceptual model without experimental validation and optimization design. Besides, the backing structure behind the absorber is not considered in the modeling, which is usually present in typical underwater applications and has been shown to affect the low-frequency underwater SA to a great extent [34]. So achieving effective broadband underwater SA in the low frequency range, typically below 2 kHz, by a subwavelength structure is still a bottle-necking challenge.

Herein, we propose a three-dimensional (3D) meta-absorber to achieve broadband underwater SA below 2 kHz. The 3D absorber consists of a plate-backed elastomer layer with a cluster of embedded scatters made of thin circular elastic plates with graded varying thickness. Unlike the conventional local resonances arising from multiple discrete single DOF mass-spring LRs, the mechanism underpinning the current design roots in the creation of multiple continuous broadband local resonant structures in form of multiple elastic plate scatters of graded thickness. While increasing the type and number of the local resonance modes, the proposed design facilitates the generation of coupled resonance modes inside the structure. Alongside the thickness gradient and the backing plate, the local dynamic of the absorber unit is enriched through enhanced modal coupling, as demonstrated by numerical simulations. By design, optimization, fabrication and experiment test, we demonstrate that the proposed meta-absorber with a deep-subwavelength thickness can deliver exceptional and even quasi-perfect SA within a broadband low-frequency range as a result of the enriched local dynamics inside the structure and coupled locally resonant responses arising from the design.

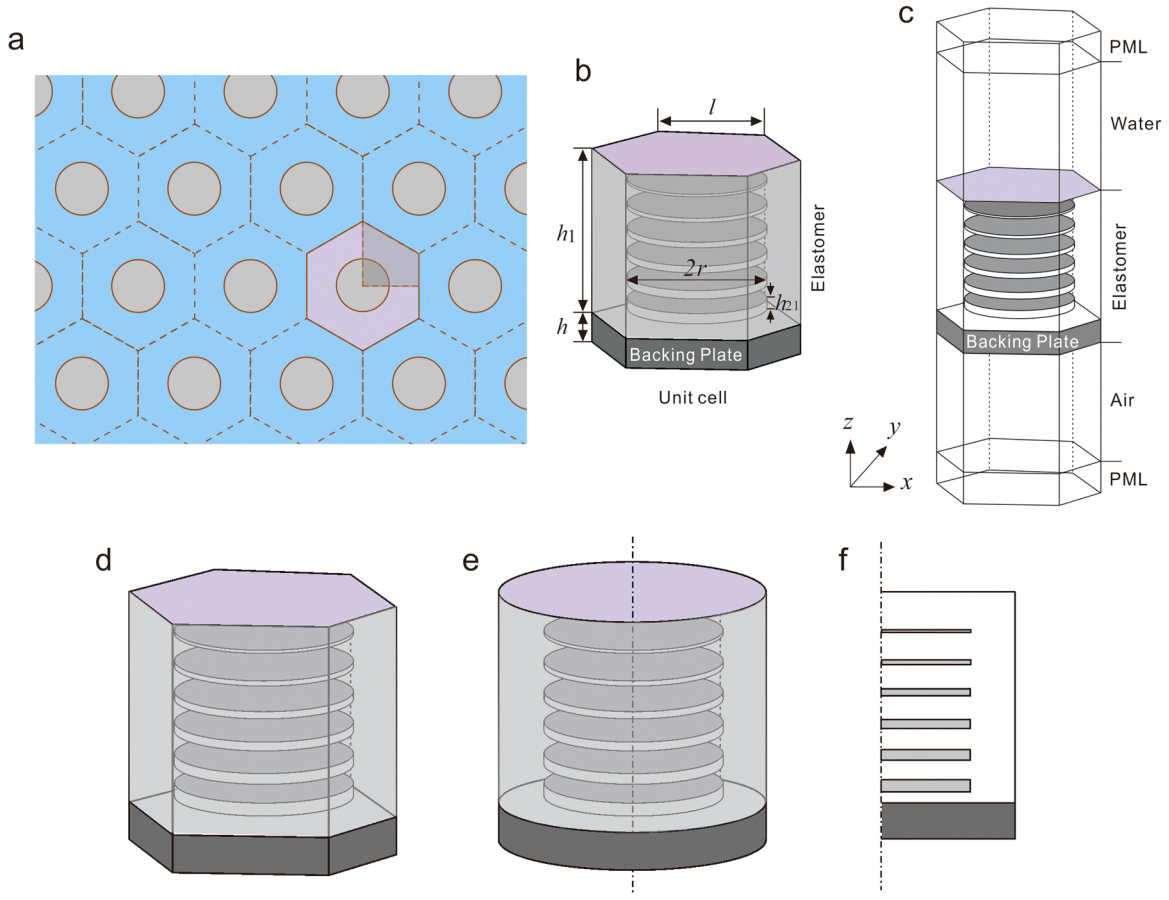

Fig. 1. Schematic diagram of the meta-absorber (a) hexagonal arrangement in vertical view, (b) a hexagonal unit cell, (c) a unit cell with upper and lower fluids, (d), (e), and (f): 3D, 3D-axisymmetric and 2D-axisymmetric models of the unit cell, respectively.

2. Three-dimensional meta-absorber modeling

The proposed meta-absorber, taking the form of a layer of steel-plate-backed elastomer with infinite size as schematically shown in Fig. 1(a), consists of hexagonal unit cells (Fig. 1(b)). The acoustic media above and beneath the meta-absorber are semi-infinite water and air, respectively (Figs. 1(c)). A plane harmonic wave is incident upon the top surface of the meta-absorber from the semi-infinite water domain. In each unit cell, I parallel thin elastic circular plate scatters (CPSs) with gradient varying thickness are inserted into the elastomer matrix. The lattice constant is l, and the radius of CPSs is r. The thickness of the ith CPS from the bottom of the absorber, h_{2i}, is varied according to

$$h_{2i} = h_{2I} + (I - i)\Delta_h, i = 1, 2, 3, \ldots I. \tag{1}$$

where Δ_h is the thickness gradient, and h_{2I} is the thickness of the Ith CPS.

The acoustic pressures in the upper and lower fluid satisfy the 3D sound wave equation:

$$\nabla^2 p = \frac{1}{c^2}\frac{\partial^2 p}{\partial t^2} \tag{2}$$

where t denotes time;p and c are the sound pressure and the associated sound speed in the fluid.

In the acoustic-structural interface, the continuity of particle displacement implies:

$$\rho\frac{\partial^2 u}{\partial t^2} = -\nabla p \tag{3}$$

where$u$ is the particle displacement.

Because of the spatial periodicity of the scatters in the meta-absorber, only a unit cell of the periodic meta-absorber needs to be modeled according to the Bloch theorem. The periodic boundary conditions can be written as:

$$\Gamma\left(x + d_x, y + d_y, z\right) = \Gamma(x, y, z)e^{j\left(kd_x sin\theta_i cos\varphi_i x + kd_y sin\theta_i sin\varphi_i y\right)}, \tag{4}$$

where Γ represents any spatial function (the sound pressure in the fluid or displacement in the structure); d_x and d_y denote the lattice sizes of a unit cell in the x and y directions, respectively; and θ and ϕ are the angles between the incident sound direction and the z-axis and between the incidence sound direction and x-axis, respectively. The reflected and transmitted sound waves can be written in the form of the sum of series as following equations:

$$p_r = \sum_{\mathrm{m}}\sum_{\mathrm{n}} R_{\mathrm{mn}} e^{-j\left(k_{\mathrm{mx}}x + k_{\mathrm{ny}}y - k_{\mathrm{mn}}z\right)}, \tag{5}$$

$$p_t = \sum_{\mathrm{m}}\sum_{\mathrm{n}} T_{\mathrm{mn}} e^{-j\left(k_{\mathrm{mx}}x + k_{\mathrm{ny}}y + k_{\mathrm{mn}}z\right)}, \tag{6}$$

where $k_{mx} = k\sin\theta_i\cos\phi_i + m\pi/d_x$, $k_{ny} = k\sin\theta_i\sin\phi_i + n\pi/d_y$ and $k_{mn} = \sqrt{k^2 - k_{mx}^2 - k_{ny}^2}$ are the acoustic wavenumbers in x, y and z directions, respectively.

The full dynamics of the 3D meta-absorber is simulated based on finite element method (FEM). The discrete governing equation for the coupled structural-acoustic problem of a unit cell in Fig. 1(c) based on FEM can be written as [35]:

$$\begin{bmatrix} \mathbf{K}_{\mathrm{s}} - \omega^2\mathbf{M}_{\mathrm{s}} & \mathbf{R}^T \\ -\rho\omega^2\mathbf{R} & \mathbf{K}_{\mathrm{f}} - \mathbf{C}_{\varnothing} - \omega^2\mathbf{M}_{\mathrm{f}} \end{bmatrix}\begin{bmatrix} u \\ p \end{bmatrix} = \begin{bmatrix} \mathrm{F}^{\mathrm{m}} \\ \mathbf{C}_0 \end{bmatrix} \tag{7}$$

where**K, C** and **M** are the stiffness, damping and mass matrix, respectively; the subscripts s and f denote the structural and fluid components, respectively; $\mathbf{C}_{\varnothing}$ and $\mathbf{C}_0$ are the nodal values of the pressure normal gradient on the fluid domain boundaries;

R is the coupling matrix describing the coupling conditions on the interface between the acoustic fluid and the structure; ρ is the fluid density and ω the angular frequency. Perfectly matched layers are adopted for both acoustic domains to simulate anechoic terminations. The modeling domain can be further simplified as a quarter of the unit cell considering the symmetry of the structure and in the case of a normal excitation. To ensure the accuracy of calculation, the maximal element size is set to be a fifth of the minimum wavelength in the material associated with the highest concerned frequencies.

By combining Eq. (7) with the periodic boundary conditions Eq. (4), the displacement u of the structure and pressure p in the fluid can be determined. The amplitudes of the reflected and transmitted sound pressuresR_{mn} andT_{mn} in Eqs. (5) and (6) can thus be obtained by applying the displacement continuity and stress equilibrium at the fluid-structural interfaces.

The sound absorption coefficient (AC) is thus calculated by

$$\alpha = 1 - R^2 - T^2 \tag{8}$$

where R and T are the reflection and transmission coefficient and can be obtained by

$$R = \sqrt{\sum_{k_{\mathrm{mn}}^2 > 0} |R_{mn}|^2}\text{and} \tag{9}$$

$$T = \sqrt{\sum_{k_{\mathrm{mn}}^2 > 0} |T_{mn}|^2} \tag{10}$$

respectively.

3. Results and discussions

The material and geometrical parameters of the each components used for the simulations are: for the elastomer layer, $h_1 = 6$cm, $\rho_1 = 580\mathrm{kg/m}^3$, $c_d = 528\sqrt{1 + j\eta_d}$ m/s, $c_s = 20\sqrt{1 + j\eta_s}$ m/s,$\eta_d = \eta_s = 0.05$, $l = 6.49$ cm with c_q and η_q being the velocities and the associated loss factors of the waves in the elastomer ($q = d$ for dilatational waves and $q = s$ for shear waves); for the CPSs, $r = 5$ cm, $\rho_2 = 7800\ \mathrm{kg/m}^3$, $E_2 = 216(1 + 0.001\mathrm{j})$ GPa, $\nu_2 = 0.3$, $I = 6$, $h_{2\mathrm{i}} \equiv 5$ mm, $i = 1, 2, \ldots, I$, for the first investigated case with six CPSs of equal thickness while $h_{2\mathrm{i}} = h_{2\mathrm{I}} + (I - i)\Delta_h$ for the case when different thickness gradient of CPSs Δ_h is introduced (under an isochoric constraint for CPSs); the backing plate (thickness $h = 1$cm) has the same material parameters as the CPSs.

3.1. Validation of the method

To verify the accuracy of the FEM model, the ACs from a uniform absorber, made of a water-loaded and plate-backed uniform elastomer without embedded CPSs, calculated by using FEM and the theoretical method [33] are plotted for comparison in Fig. 2. Note a plane harmonic wave with a normal impinging angle from the semi-infinite water domain is considered in the present and following calculations. As shown in Fig. 2, the ACs from the two methods demonstrate excellent agreement, thus verifying the FEM model. It is also noticed that the ACs from the uniform absorber without CPSs show relatively low absorption in the concerned frequency range with a peak value of 0.41 at $f = 900$ Hz. This peak corresponds to the resonance of the water-elastomer-backing plate system, acting as a mass-spring-mass resonator [36,37]. In a way, this shows the existing challenges facing the conventional sound absorber design.

3.2. Absorption from 3D meta-absorber

The ACs from the 3D meta-absorber with the embedded CPSs are then shown in Fig. 3. The case with six CPSs of equal thickness is first investigated. It is observed that compared with the uniform absorber without the embedded CPSs, AC from the meta-absorber is enhanced

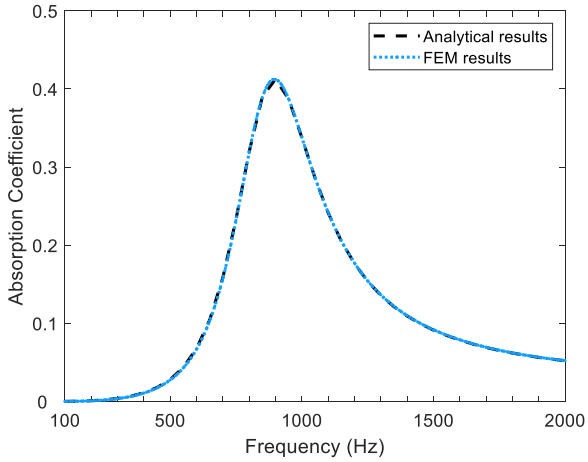

Fig. 2. Comparison of absorption coefficients of a uniform elastomer with a backing plate by using FEM and theoretical method.

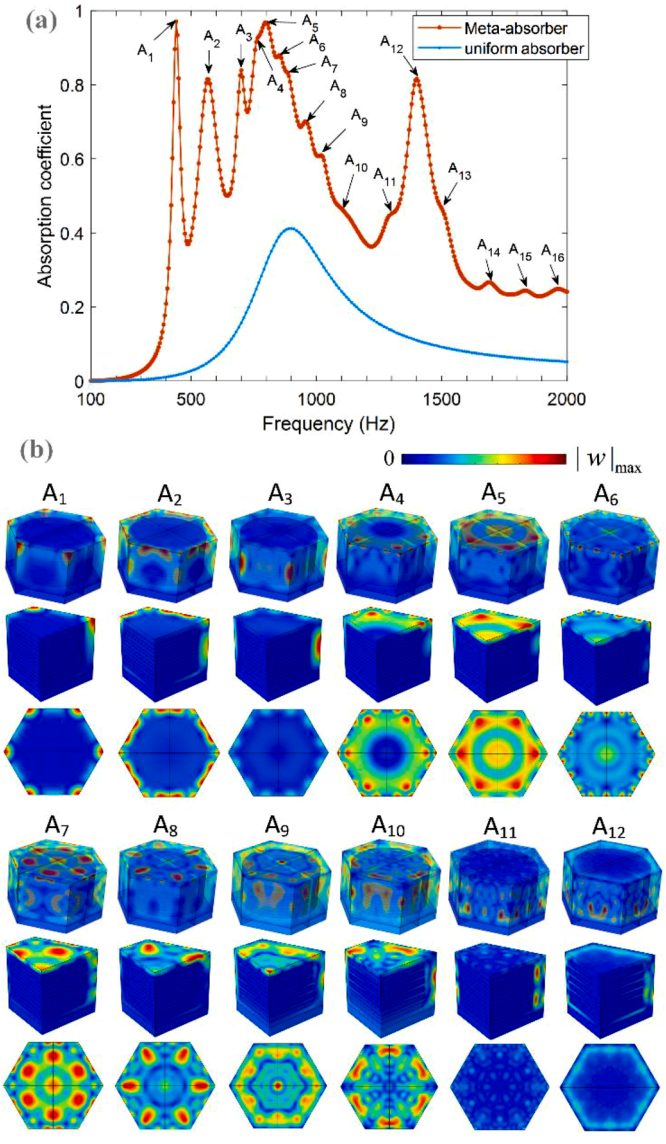

Fig. 3. (a) Absorption coefficients from the meta-absorber and the uniform absorber counterpart. (b) Displacement fields corresponding to the first twelve absorption peaks (upper row: the whole unit cell, middle row: one eighth of the unit cell, and lower row: the top surface of the unit cell).

within the entire frequency range with multiple absorption peaks where high or quasi-perfect absorptions are achieved. Especially, nearly perfect absorption (over 97%) is observed at 440 Hz, where the meta-absorber thickness is merely 1.8% of the incident sound wavelength, $\lambda_w (= c_w/f)$, namely at a deep-subwavelength scale.

To identify these peaks and understand the underlying physics, the displacement fields at these frequencies corresponding to the first twelve peaks A_1-A_{12} are examined in Fig. 3(b) (upper row: the whole unit cell; middle row: one eighth of the unit cell; and lower row: the top surface of the unit cell). It is observed in Fig. 3(b) that such a unit cell exhibits very rich and different resonance patterns at different frequencies. For low-frequencies peaks A_1-A_3, significant vibration occurs mainly around the corners, edges, or both corners and edges of the upper side of the meta-absorber, respectively, and can be loosely classified as corner modes and edge modes. As the frequency increases, energetic vibration deformation starts to appear at the upper surface of the meta-absorber to form surface modes. With further increase in frequency, they eventually involve more obvious deformation from the corner, edge, and surface of the unit to form more complex hybrid resonance patterns, exemplified by A_4-A_{10}. For even higher frequencies (A_{11}-A_{13}), significant vibration is also noticed inside the meta-absorber to form body modes, in which strong dynamics are also observable in the elastomer part between the CPSs. Note that the vibration patterns associated with two peak series, A_4-A_{10} and with A_{11}-A_{13}, are due to the coupling among different modes (corner, edge, and surface). For each series, the resonance frequencies are closely spaced, and the corresponding vibration displacement shows resembling resonance patterns. As a result, this enriches modal coupling to yield complex system dynamics inside the unit, which is responsible for the high and quasi-perfect behavior at multiple frequencies and within a broad low-frequency range at a deep subwavelength thickness.

Then, a linear thickness gradient of the CPSs is introduced to evaluate how it would affect the SA of the meta-absorber. Fig. 4 shows the ACs for different thickness gradients Δ_h. To ensure fair comparisons, the total weight and the radius of the CPSs are kept the same or an isochoric constraint for CPSs is imposed. One can observe that as Δ_h increases, SA peaks are generally shifted to lower frequencies to different degrees, more significantly for higher-frequency peaks than for lower ones. Hence, the peaks within the frequency range of interest are getting closer and the coupling among the corresponding locally resonant modes becomes stronger, resulting in high SA with broader frequency band in the presence of thickness gradient (blue and orange curves in Fig. 4). This indicates the thickness gradient offers an extra degree of freedom for adjusting the effect of coupling among local resonance

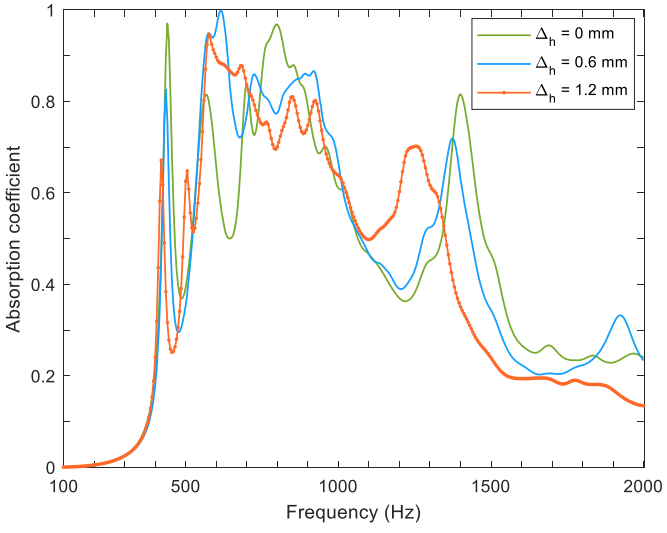

Fig. 4. Variations of absorption coefficients with thickness gradient of the embedded CPSs.

modes in views of altering the AC.

3.3. Simplified 2D-axisymmetric model

Considering that 3D simulation is time-consuming, a simplified 2D-axisymmetric model of the meta-absorber is thus considered, verified and utilized to 1) separate the effects of the 3D absorption with 2D ones for better physical understanding, and 2) facilitate subsequent optimization of meta-absorbers. The simplified 2D-axisymmetric model, commonly adopted to symmetric structure with symmetric inner scatters and excitations, is schematically shown in Fig. 1(f). The model is obtained by approximating the hexagonal cell (Fig. 1(d)) by a cylindrical one (Fig. 1(e)), considering the symmetries of both the CPSs and the elastomer. For this model, vanishing normal displacement is required at the outer boundary of the 2D cell or $\mathbf{u} \bullet \mathbf{n} = 0$ considering both the periodicity and the symmetry of the structure. For conventional absorbing materials with cavities, the ACs calculated by the 2D-axisymmetric model have been shown to converge to those from the 3D counterpart when sufficient amount of damping loss is introduced in the absorbing matrix [38]. Validations of such a simplification for different inner structures, however, are still lacking. Here, the 3D model is compared with the 2D-axisymmetric model in terms of sound absorption for different shear loss factors, with results shown in Figs. 5.

As shown in Fig. 5(a), with a small loss factor $\eta_s = 0.05$, differences in SA from the two models are obvious. Two AC peaks A_1 and A_3 which appear in the 3D model are unobservable for the 2D-axisymmetric model; while the small SA peak A_{14} observed in the 3D model becomes much more pronounced for the 2D model. One plausible reason behind is that the vibration of the meta-absorber corresponding to A_1, A_3 and A_{14}, as calculated by the 3D model, is dominated by the corner mode (A_1) and edge mode along the vertical edge of the hexagonal cell (A_3 and A_{14}), respectively, as shown in Fig. 3(b) and Fig. S1. These modes are typical and specific to the hexagonal column which is absent in the axisymmetric cylindrical model. While for other peaks except A_1, A_3 and A_{14}, vibration energy is concentrated on the surface, at non-vertical edge or across the entire mode of the unit cell or body mode, which are shared by both models. Hence, the absorption mainly differs at these three peaks. As η_s gradually increases, the SA peaks corresponding to corner mode- or vertical edge mode-dominated A_1, A_3 and A_{14} are greatly reduced (compare Figs. 5(a) with 5(b), 5(c) and 5(d)). Thus, the SA curves from the two models are getting closer. For η_s= 0.35 and higher, the differences between the two models are nearly negligible, as shown in Figs. 5(c) and 5(d). Therefore, the 2D-axisymmetric model is deemed representative enough of the meta-structure, which will be used as a simplified model for AC calculation and optimization hereafter.

3.4. Effect of the backing plate

The effect of the backing plate on SA is investigated based on the verified 2D axisymmetric model. A relatively high shear loss factor or η_s = 0.35 (with η_d=0.2) is assigned to guarantee the consistence between the 3D and the simplified 2D-axisymmetric models. A detailed parameter survey associated with other materials and geometrical parameters of the meta-absorber based on the simplified 2D model can be referred to Figure. S3 in the *supplementary materials*.

Fig. 6(a) shows the variation of ACs without/with a backing plate of different thicknesses. Here an equal thickness is assigned to all CPSs for better clarification of the effect of the backing plate itself. Results show significant effects of the backing plate. Without the backing, the first SA peak occurs at a relatively low frequency f = 375 Hz where the absorption is dominated by the bending of the elastomer part without the embedded PSs with nearly clamped-clamped boundaries, as shown by the displacement distribution map in Fig. 6(b). Besides, the displacement maps associated with the first three SA peaks show different vibration patterns, as shown by Figs. 6(b)−6(d). With the introduction of the backing plate, the first two SA peaks are shifted to high frequencies and the third peak to lower frequencies so that the first three peak frequencies become closer, resulting in high absorption across a broad frequency band (see orange and yellow curves in Fig. 6) due to the enhanced coupling among these resonance modes induced by the

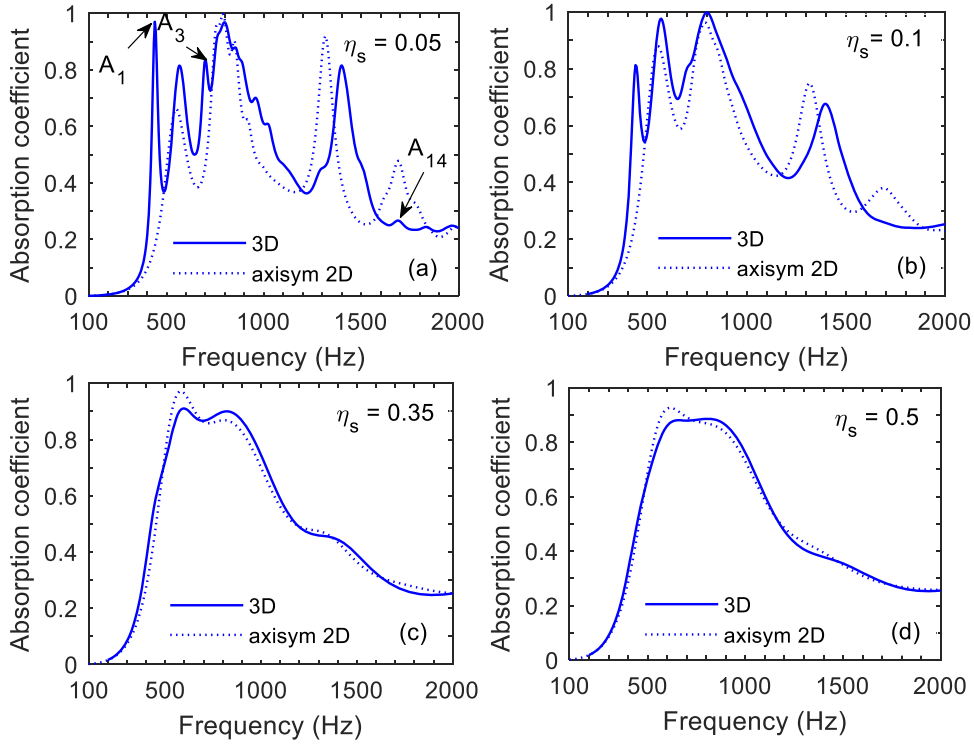

Fig. 5. Variations of absorption coefficients with shear wave loss factor η_s, for all cases η_d=0.05. The solid and dotted curves represent the 3D and axisymmetric 2D models, respectively.

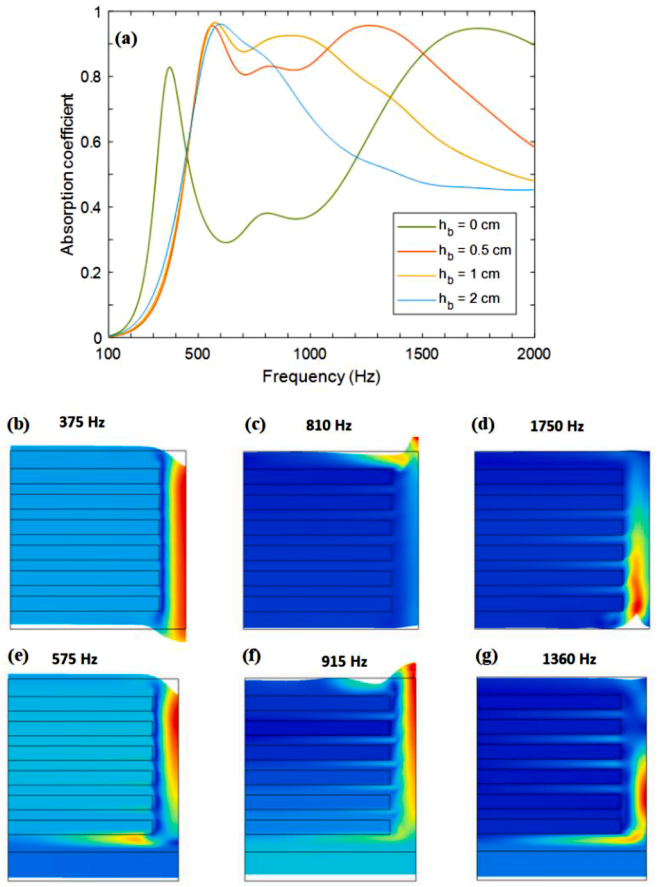

Fig. 6. Absorption coefficients of the 2D meta-absorber with backing plate of different thicknesses (a), and displacement fields at the first three SA peaks of the absorber without ((b)-(d)) and with ((e)-(g)) the backing plate (h_b = 0.5 cm), with η_d=0.2. η_s= 0.35 for all cases.

backing plate, as demonstrated by the resembling resonance responses at these peak frequencies with the backing (Figs. 6(d), (e) and (f)). This observation testifies the positive role that the backing plate plays in promoting the modal coupling in the meta-absorber unit, which cannot be neglected when designing the meta-absorber.

4. Design and optimization

An optimal design of meta-absorbers is further conducted based on the verified 2D-axisymmetric model combined with Nelder–Mead algorithm to achieve the optimal SA performance across a broad low-frequency range. Nelder–Mead algorithm is a gradient-free algorithm often applied to nonlinear optimization problems for which derivatives of the objective functions may not be known. The algorithm relies on a simplex of $N+1$ points, with N being the number of control variables. In each iteration, it uses reflection, expansions and contractions to improve the worst point in the simplex.

The thickness of the elastomer and that of the backing plate are fixed at 6 cm and 1 cm, respectively. To balance the average and the worst performance across the frequency range of interest, two quantities are considered to measure the ultimate objectives: the average of the quadratic reflection coefficient and the quadratic transmission coefficient $J_1(\mathbf{V}) = \frac{1}{n_f}\sum_{k=1}^{n_f}(R^2(\mathbf{V},f_k) + T^2(\mathbf{V},f_k))$, and their maxima $J_2(\mathbf{V},f) = \max((R^2(\mathbf{V},f),\ T^2(\mathbf{V},f))_{f\in(f_1,f_2)}$, where $n_f = (f_2 - f_1)/\Delta f + 1$ is the total number of discrete frequencies in the concerned range and Δf is the frequency step used in the optimization. Here Δf equals to 100 Hz and f_2 and f_1 to 200 Hz and 2000 Hz respectively; $\mathbf{V}$ represents the set of design variables:

$$\mathbf{V} = [r,\ h_2, \rho_c,\ c_{d0},\ c_{s0}, \eta_d,\ \eta_s, \Delta h], \tag{11}$$

which are constrained by $r \in [1, 5.8]$cm, $h_2 \in [1, 8]$mm, $\rho_c \in [500, 1000]$ kg/m^3,$c_{d0} \in [3001000]m/s$, $c_{s0} \in [10100]m/s$, $\eta_d \in [0.051]$, $\eta_s \in [0.11]$ and $\Delta h \in [-0.02, 0.02]$ mm.

The objective function chosen for this optimization problem, combining the two quantities defined above, writes:

$$J(\mathbf{V},f) = \sum_{i=1}^{2} q_i J_i(\mathbf{V},f), \tag{12}$$

where q_i is a weighting factor. Two weighting strategies are selected. The first one is an average weighting strategy to all concerned frequencies called strategy 1 (Str. 1) where $q_1 = q_2 = 0.5$. Since the working frequency band for applications like sonar detection tends to be as low as a few hundred Hz where the low-frequency SA performance is more challenging and desirable for underwater stealth purpose, the second weighting strategy 2 (Str. 2) is proposed through increasing the weighting of the low-frequency in the defined objective function with $q_i = 0.5\frac{\Delta f}{f}\left(\frac{1}{n_f}\sum_{k=1}^{n_f} J\right) \Big/ \bar{J}_i$, where $\bar{J}_i = \frac{1}{n_f}\sum_{k=1}^{n_f} J_i$ is the average of J_i, i =1, 2 over the concerned discrete frequency points whose total number is denoted by n_f as mentioned before and $\bar{J}_1 = J_1$; the physical quantity in the parenthesis represents the average of J over the concerned frequencies. The initial values of the design variables are set according to the parametric study results presented in the supplementary materials as: r = 2cm, h_2 = 5mm, ρ_c = 500kg/m^3,$c_{d0} = 300m/s$,$c_{s0} = 10m/s$, $\eta_d = 0.7$, $\eta_s = 0.35$ and $\Delta h = 0$ mm. The two strategies take 2 hours 53 mins and 3 hours 20 mins, respectively, to complete an exhaustive search over the concerned multi-frequency range using the same computational facility (Workstation with Xeon(R) 5222 CPUX2, 128 Gb memory, Win10 64 bit). This is deemed reasonable for the multi-frequency optimization of such a complex structure involving fluid-structure interaction.

It is noted that the applied Nelder-Mead algorithm walks toward improving the nonlinear objective function values by iteratively replacing the worst corner of a simplex in the design variable space. However, the algorithm can converge prematurely at a suboptimal solution when the simplex shape degenerates or collapses along one direction. To avoid the solution to be trapped in a suboptimal solution, a restart procedure is included in the algorithm via using simplex gradient to detect stagnation and determine the orientation of the new simplices whenever the geometry or poisedness of the simplex vertices deteriorates [39].

The optimized design variables based on the two strategies are listed in Table 1, with corresponding ACs shown in Fig. 7. For both strategies, high SAs are obtained around the target frequencies. For the average weighting strategy 1, high SAs (>0.8) are observed within an ultra-broad low-frequency band from 440 to 2000 Hz. Excellent SAs (>0.9) are observed from 500 to 2000 Hz with an average AC up to 0.952.

For weighting strategy 2, the high SA region is shifted to a lower frequency range as imposed by the applied optimization strategy by exerting a higher weighting to the lower frequencies. For this case, high SAs (>0.8) are noticed from 350 Hz to 1530 Hz. Notably, nearly perfect absorption (>0.97) is observed at around 415 Hz where the meta-absorber thickness is merely 1.7% of λ_w. Meanwhile, the SA is above 0.79 within an ultra-broad frequency range from 345 Hz until 2 kHz, with an average AC of 0.878.

5. Experimental validation

A meta-absorber prototype was then manufactured using rubber, steel plates and epoxy adhesive. A cylinder container mold was first designed to facilitate the positioning of the embedded CPSs. The sample

Table 1
Optimized parameters of the meta-absorber.

	r(mm)	h_2(mm)	Δh (mm)	ρ_c(kg/m^3)	c_{d0}(m/s)	c_{s0}(m/s)	η_d	η_s
Str. 1	54.714	7.995	2e-5	572.27	334.72	10.032	0.99	0.64
Str. 2	53.42	7.999	2e-5	595.18	300.15	10.004	0.654	0.433

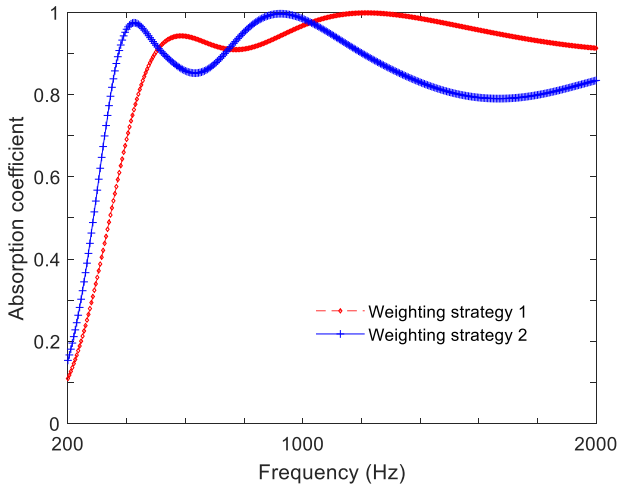

Fig. 7. Absorption coefficients of the meta-absorber with optimized designs.

was then formed by placing six steel CPSs horizontally into the mold before pouring rubber materials. Epoxy adhesive was added over the surface of the steel plates before they are placed into the mold. The manufactured sample is 60 mm thick with a diameter of 118 mm. A steel backing plate, 9.1 mm thick, was finally pasted on the bottom of the sample with the same diameter.

Note that the meta-absorber prototype sample was designed according to the optimized results. However, in the process of practical sample manufacturing, it was difficult to find/manufacture a rubber sample with the exact parameters as the optimized values. Thus, the material parameters of the manufactured rubber sample were measured by a Dynamic Mechanical Analyzer to make sure the theoretical and measured parameters are as close as practically possible. The Young's modulus and the loss factor of the rubber were measured by MetraviB Dynamic Mechanical Analyzer+450. Other parameters of the sample used in the experiment are: r = 5cm, $h_{2i} \equiv$ 3 mm (i= 1, 2 , …, 6), ρ_2 = 7800kg/m^3, E_2 = 216(1+0.001j) GPa, and ν_2=0.3 for the CPSs; ρ_c = 1030kg/m^3,Poisson ratio ν = 0.495 [27,40] for the rubber matrix. The velocities and the loss factors associated with the dilatational and shear waves of the rubber were obtained from the complex Young's modulus and the Poisson ratio [41].

To guarantee an accurate positioning of the CPSs, the manufactured sample was scanned using a 3D CT Metrology scanner phoenix v|tome|x m. The scanned 3D image and the side view image of the meta-absorber sample are shown in Figs. 8(c) and 8(d), with the designed and fabricated one shown in Figs. 8(a) and 8(b). Considering the equivalence between a large absorber sample under normal acoustic incidence and a small sample inside an impedance tube, the AC of the sample was then tested in a hydroacoustic impedance tube using transfer function method within a frequency range of 500 Hz~6 kHz. The length and the inner diameter of the tube are 5 m and 120 mm, respectively. A schematic showing the hydroacoustic impedance tube, the experimental setup and test principle is given in Fig. 8(e). The absorption coefficient is obtained based on transfer function method using two microphones. The transfer function can be obtained by $\mathbf{H} = p_2/p_1$, where p_1 and p_2 are the acoustic pressure measured by the upper and lower hydrophones. The complex pressure reflection coefficient is thus calculated by [42]:

$$R = \frac{\mathbf{H}e^{jk_w L} - e^{jk_w(L+d)}}{e^{-jk_w(L+d)} - \mathbf{H}e^{-jk_w L}}. \tag{13}$$

where k_w=$2\pi f/c_w$ is the acoustic wavenumer in water.

Therefore, the absorption coefficient can be obtained by $\alpha = 1 - |R|^2$. The measured results are then compared with the predicted ones based on the 2D-axisymmetric model in Fig. 9, showing a general agreement and expected high absorption (>0.82 on average) from 800 Hz to 6000 Hz. Notably, quasi-perfect absorption is also observed from both simulation (0.976) and experiment (0.94) at 1000 Hz with an absorber thickness of $\lambda_w/25$, confirming the subwavelength and quasi-perfect absorption feature of the meta-absorber for low-frequency underwater sound absorption. Observed discrepancies between the simulation and experiment can be attributed to the differences in boundary conditions used in the simulation and experiment (an approximately free boundary of the sample is set in the hydroacoustic impedance tube). Nevertheless, experiment confirms the efficacy of the proposed meta-absorber design

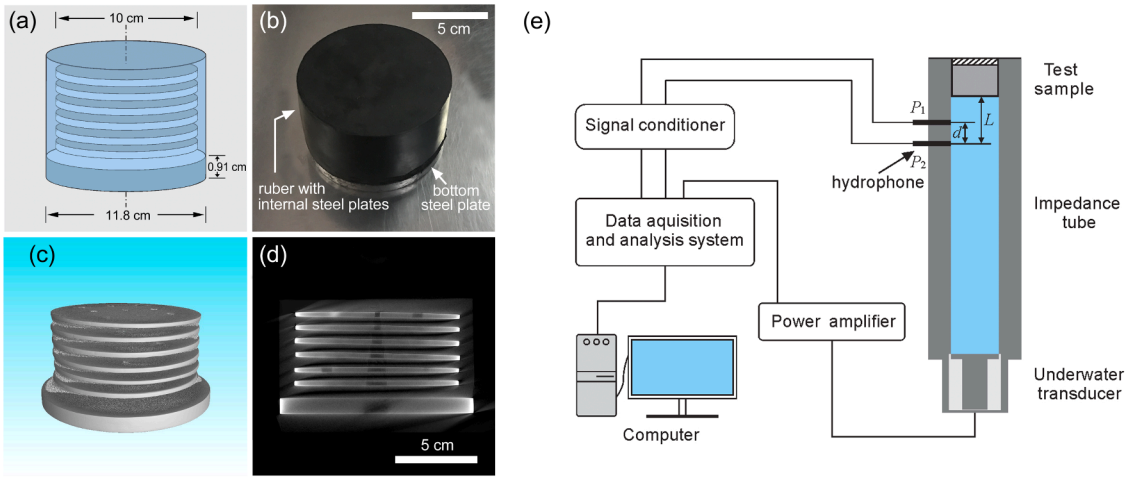

Fig. 8. Designed (a) and manufactured (b) meta-absorber. 3D image (c) and side view image (d) of the meta-absorber sample through CT scanning using Phonenix v | tome| x m. (e) Schematic of the hydroacoustic impedance tube experimental setup and test principle.

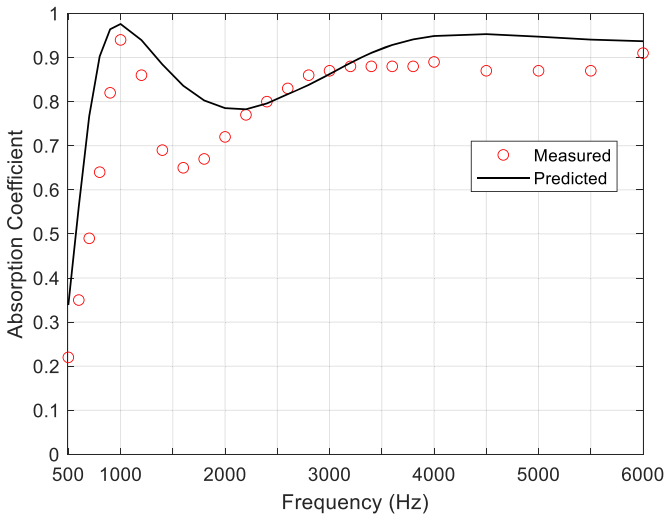

Fig. 9. Comparisons of the predicted and measured absorptions.

in terms of sound absorption.

6. Conclusions

Recent advent in acoustic metamaterials to achieve subwavelength and quasi-perfect absorption has aroused great interest in physical and engineering communities but is mainly limited to air-borne sound control. Since waterborne sound has much longer wavelength, lower dissipation and closer impedance to solids, the design of meta-structure for underwater sound absorption is a long-lasting challenge. Current underwater sound absorbers merely work at broadband high frequencies (typically above 2 kHz) or narrowband low frequencies (by introducing discrete narrowband spring-mass local resonators (LRs)). Efficient absorption of broadband low-frequency underwater sound using a deep-subwavelength structure is therefore an important yet challenging issue. To tackle the challenge, this paper proposes the design of a novel meta-absorber, consisting of multiple thickness-graded CPSs embedded into an elastomer matrix layer backed by a metallic plate. CPSs act as continuous local resonators, which, through thickness gradient and with elastomer and the backing plate acting as agent, create rich local dynamics and enhanced coupled local responses inside the meta-absorber unit. The former is evidenced by the creation of diverse types of modes such as corner, edge, surface and body modes inside the meta-absorber unit; the latter by the enhanced coupling among closely spaced local modes. The combined effect yields high and quasi-perfect absorption at multiple frequencies or over a broad low-frequency range. To achieve ultimate SA performance, an optimization design of the geometrical parameters of the CPSs and material parameters of the elastomer matrix is conducted. Experimental results demonstrate and confirm excellent and broadband low-frequency SA, in agreement with numerical predictions. This research offers a novel and effective solution to low-frequency underwater sound absorption, which may open a new avenue to broadband low-frequency sound control based on a deep-wavelength structure.

As a final remark, one should take note that the case of CPSs with a linear thickness variation across the absorber is considered to show the effects of the thickness variation/gradient of the CPSs on SA properties. This simple yet representative configuration serves the purposes of illustrating that embracing the idea of panel thickness variation in the design offers an extra degree of freedom for adjusting the coupling among local resonance modes so as to create a positive effect on SA. There exist no technical obstacles to examine other types of thickness variation (e.g. quadratic or a power law-based) under the analysis umbrella proposed in this work, which can possibly further improve the SA upon proper optimization. We believe the underlying physics will remain the same, and this might be investigated as a future work.

Declaration of Competing Interest

The authors declare that they have no known competing financial interests or personal relationships that could have appeared to influence the work reported in this paper.

Acknowledgements

This work was supported by the National Natural Science Foundation of China (Grant Nos. 11874303, 11504324), Equipment Pre-Research Field Fund (Grant Nos. 80910010102) and Fundamental Research Funds for the Central Universities (No. AE 89991/318).

Supplementary materials

Supplementary material associated with this article can be found, in the online version, at doi:10.1016/j.ijmecsci.2021.106732.

References

[1] Cummer SA, Christensen J, Alù A. Controlling sound with acoustic metamaterials. Nat Rev Mater 2016;1:1–13.
[2] Mei J, Ma G, Yang M, Yang Z, Wen W, Sheng P. Dark acoustic metamaterials as super absorbers for low-frequency sound. Nat Commun 2012;3:756.
[3] de Sousa AC, Deckers E, Claeys C, Desmet W. On the assembly of Archimedean spiral cavities for sound absorption applications: design, optimization and experimental validation. Mech Syst Signal Process 2021;147:107102.
[4] Liu X, Wang C, Zhang Y, Huang L. Investigation of broadband sound absorption of smart micro-perforated panel (MPP) absorber. Int J Mech Sci 2021;199:106426.
[5] Tang Y, He W, Xin F, Lu TJ. Nonlinear sound absorption of ultralight hybrid-cored sandwich panels. Mech Syst Signal Process 2020;135:106428.
[6] Lee YY. The effect of leakage on the sound absorption of a nonlinear perforated panel backed by a cavity. Int J Mech Sci 2016;107:242–52.
[7] Ma F, Chen J, Wu JH. Time-delayed acoustic sink for extreme sub-wavelength focusing. Mech Syst Signal Process 2020;141:106492.
[8] Lee YY, Lee EWM. Widening the sound absorption bandwidths of flexible micro-perforated curved absorbers using structural and acoustic resonances. Int J Mech Sci 2007;49:925–34.
[9] Yang C, Cheng L. Sound absorption of micro-perforated panels inside compact acoustic enclosures. J Sound Vib 2016;360:140–55.
[10] Zhang Y, Chen K, Hao X, Cheng Y. A review of underwater acoustic metamaterials. Chin Sci Bull 2020;65:1396–410.
[11] He Z, Zhao Y. Fundamental of acoustic theory (in chinese). Beijing: National Defense Industry Press; 1981.
[12] Meyer E, Brendel K, Tamm K. Pulsation oscillations of cavities in rubber. J Acoust Soc Am 1958;30:1116–24.
[13] Ivansson SM. Numerical design of Alberich anechoic coatings with super-ellipsoidal cavities of mixed sizes. J Acoust Soc Am 2008;124:1974–84.
[14] Leroy V, Strybulevych A, Lanoy M, Lemoult F, Tourin A, Page JH. Super-absorption of acoustic waves with bubble meta-screens. Phys Rev B 2015;91:020301.
[15] Hinders MK, Rhodes BA, Fang TM. Particle-loaded composites for acoustic anechoic coatings. J Sound Vib 1995;185:219–46.
[16] Baird AM, Kerr FH, Townend DJ. Wave propagation in a viscoelastic medium containing fluid-filled microspheres. J Acoust Soc Am 1999;105:1527–38.
[17] Zhao H, Liu Y, Yu D, Wang G, Wen J, Wen X. Absorptive properties of three dimensional phononic crystal. J Sound Vib 2007;303:185–94.
[18] Zhao H, Zong L, Hong W, Long Y, Gang W, Sen W. Sound absorption of locally resonant sonic materials. Chin Phys Lett 2006;23:2132–4.
[19] Wen J, Zhao H, Lv L, Yuan B, Wang G, Wen X. Effects of locally resonant modes on underwater sound absorption in viscoelastic materials. J Acoust Soc Am 2011;130:1201–8.
[20] Naify CJ, Martin TP, Layman CN, Nicholas M, Thangawng AL, Calvo DC, Orris GJ. Underwater acoustic omnidirectional absorber. Appl Phys Lett 2014;104:073505.
[21] Feng Y, Qiao J, Li L. Acoustic behavior of composites with gradient impedance. Mater Des 2020;193:108870.
[22] Cheng G, He D, Shu G. Underwater sound absorption property of porous aluminum. Colloid Surface A 2001;179:191–4.
[23] Wang X. Porous metal absorbers for underwater sound. J Acoust Soc Am 2007;122:626–35.
[24] Xu W, Jiang C, Zhang J. Improvement in underwater acoustic absorption performance of open-celled SiC foam. Colloid Surface A 2015;482:568–74.
[25] Liu Z, Zhang X, Mao Y, Zhu YY, Yang Z, Chan CT, Sheng P. Locally resonant sonic materials. Science 2000;289:1734–6.
[26] Meng H, Wen J, Zhao H, Wen X. Optimization of locally resonant acoustic metamaterials on underwater sound absorption characteristics. J Sound Vib 2012;331:4406–16.

[27] Shi K, Jin G, Liu R, Ye T, Xue Y. Underwater sound absorption performance of acoustic metamaterials with multilayered locally resonant scatterers. Results Phys 2019;12:132–42.
[28] Jiang H, Wang Y. Phononic glass: a robust acoustic-absorption material. J Acoust Soc Am 2012;132:694–9.
[29] Jiang H, Wang Y, Zhang M, Hu Y, Lan D, Zhang Y, Wei B. Locally resonant phononic woodpile: a wide band anomalous underwater acoustic absorbing material. Appl Phys Lett 2009;95:104101.
[30] Sharma GS, Skvortsov A, MacGillivray I, Kessissoglou N. Sound absorption by rubber coatings with periodic voids and hard inclusions. Appl Acoust 2019;143:200–10.
[31] Jin G, Shi K, Ye T, Zhou J, Yin Y. Sound absorption behaviors of metamaterials with periodic multi-resonator and voids in water. Appl Acoust 2020;166:107351.
[32] Wang Z, Huang Y, Zhang X, Li L, Chen M, Fang D. Broadband underwater sound absorbing structure with gradient cavity shaped polyurethane composite array supported by carbon fiber honeycomb. J Sound Vib 2020;479:115375.
[33] Zhang Y, Pan. K. Chen J, Zhong J. Subwavelength and quasi-perfect underwater sound absorber for multiple and broad frequency bands. J Acoust Soc Am 2018;144:648–59.
[34] Zhao H, Wen J, Yang H, Lv L, Wen X. Backing effects on the underwater acoustic absorption of a viscoelastic slab with locally resonant scatterers. Appl Acoust 2014;76:48–51.
[35] Hennion AC, Decarpigny JN. Analysis of the scattering of a plane acoustic wave by a doubly periodic structure using the finite element method: application to Alberich anechoic coatings. J Acoust Soc Am 1991;90:3356–67.
[36] Zhang Y, Pan J. Underwater sound scattering and absorption by a coated infinite plate with a distributed inhomogeneity. J Acoust Soc Am 2013;133:2082–96.
[37] Zhang Y, Huang H, Zheng J, Pan J. Underwater sound scattering and absorption by a coated infinite plate with attached periodically located inhomogeneities. J Acoust Soc Am 2015;138:2707–21.
[38] Zhong J, Zhao H, Yang H, Yin J, Wen J. On the accuracy and optimization application of an axisymmetric simplified model for underwater sound absorption of anechoic coatings. Appl Acoust 2019;145:104–11.
[39] Conn AR, Scheinberg K, Vicente LN. Introduction to derivative-free optimization. MPS-SIAM Series on Optimization, SIAM; 2009.
[40] Wen J, Yu D, Zhao H, Cai L, Xiao Y, Wang G, Yin J. Artificial propagation of elastic waves in periodic structures: vibration and acoustic characteristics. Chinese Edition. Beijing: China Science Publishing Company; 2015.
[41] Ko SH, Pyo S, Seong W. Structure-Borne and flow noise reductions (Mathematical modeling). Seoul: Seoul National University Press; 2001.
[42] Chung JY, Blaser DA. Transfer function method of measuring in-duct acoustic properties. I. Theory. J Acoust Soc Am 1980;68:907–13.